CHEMISTRY OF MATERIALS

pubs.acs.org/cm Article

$LiIn_2SbO_6$: A New Rutile-Related Structure Type with Unique Ion Channels

Steven Flynn, Sheel Sanghvi, Matthew L. Nisbet, Kent J. Griffith, Weiguo Zhang, P. Shiv Halasyamani, Sossina M. Haile, and Kenneth R. Poeppelmeier*

Cite This: *Chem. Mater.* 2020, 32, 4785–4794 Read Online

ACCESS | Metrics & More | Article Recommendations | Supporting Information

ABSTRACT: Single crystals of $LiIn_2SbO_6$ (LIAO) have been synthesized using a Li_2MoO_4 flux and characterized with X-ray diffraction. The compound crystallizes in a new structure type with a rutile-related framework. Like others in the rutile-related family, LIAO is formed of chains of edge-sharing octahedra. The chain structure, with a width that alternates between single and double octahedra, has not previously been reported in a rutile-related material. The framework is formed via corner sharing by the chains in a checkerboard arrangement, with Li^+ residing in tetrahedral sites in the resulting, identically-alternating channels. Solid-state $^{6/7}Li$ NMR spectroscopy and ab initio spectral calculations verify the presence of tetrahedrally coordinated lithium. The solution determined here contradicts previous reports of this material as a cation-ordered variant of $LiSbO_3$. The relationship between this new structure and $LiSbO_3$ and others in the rutile-related family is discussed. Variable temperature powder X-ray diffraction and diffuse reflectance show that LIAO has high thermal stability and a large direct band gap of 3.9 eV. AC impedance spectroscopy reveals that LIAO is a relatively poor Li conductor, displaying a conductivity of 1.3×10^{-7} S/cm at 623 K, along with an activation energy for charge transport of 1.1 eV. This material presents an opportunity to explore a new subfamily of rutile-related materials in which alternating-width chains may provide an independent avenue for tuning desired properties.

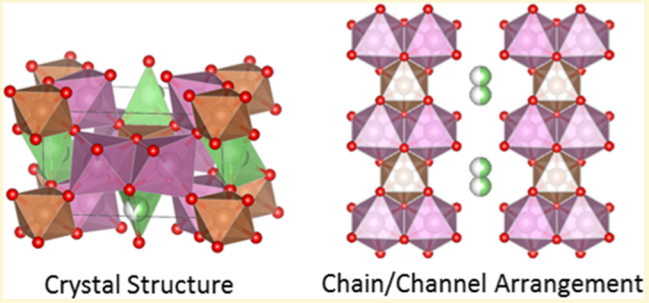

INTRODUCTION

Rutile-related phases make up a diverse materials family that has long been of great interest to researchers as catalysts, photoanodes, battery materials, ion conductors and for capture of contaminants such as radioactive isotopes.[1−13] These compounds are related by their shared structural motif of corner-sharing chains composed of edge-sharing octahedra and a framework stoichiometry of MX_2. They differ, however, in the arrangement or width of their chains, by the presence or lack of ions in the channels between chains, and in their chemical composition.[1,2] As such, this family encompasses structures as wide-ranging as rutile, ramsdellite, hollandite, psilomelane, and many others.[1−5]

One important subset of rutile-related materials that has been the subject of a dedicated research focus is the Li-containing group. The characteristic channels of these compounds are theoretically conducive to high Li capacities (335 mA h/g in ramsdellite-type TiO_2) and relatively high Li mobilities owing to an unobstructed diffusion path.[9,14] In electrolytic manganese dioxide, a disordered intergrowth of pyrolusite (rutile-type) and ramsdellite, these properties have led to successful application as a cathode in lithium and alkaline batteries.[4,5] Numerous theory-based and experimental studies have utilized the diversity of structures in the rutile-related family to probe the dependency on the channel size and structure type of parameters central to their possible performance as battery components, including the preferred sites of Li occupancy in tetrahedral versus octahedral versus framework sites and stability with respect to structural transitions and hydrolysis.[4−10,12−19] As such, the discovery of an entirely new Li-containing channel structure is valuable to this community by offering additional insight into previous studies and opportunities for designing solid-state Li-battery components.

Here, we present the crystal structure of $LiIn_2SbO_6$ (lithium indium antimony oxide or LIAO), which adopts a previously unreported rutile-related structure with *Pnnm* symmetry. This conflicts with earlier reports of LIAO which describe it as cation-ordered $LiSbO_3$ in the *Pnn*2 space group without providing a full structural solution.[20−22] We identify the source of this discrepancy as an unrecognized shift of Li^+ into

Received: April 7, 2020
Revised: May 6, 2020
Published: May 7, 2020

https://dx.doi.org/10.1021/acs.chemmater.0c01491
Chem. Mater. 2020, 32, 4785–4794

Table 1. Crystallographic Data for LIAO

compound	$LiIn_2SbO_6$		
ICSD code	1976009	1976010	1976011
temperature, K	99.96	323.0	500.01
λ, Å	0.71073	0.71073	0.71073
space group (no.)	*Pnnm* (58)	*Pnnm* (58)	*Pnnm* (58)
unit cell			
a, Å	5.0902(4)	5.0991(2)	5.1170(3)
b, Å	5.3328(4)	5.3298(2)	5.3335(3)
c, Å	8.8813(6)	8.8729(3)	8.8794(6)
V, Å^3	241.08(3)	241.140(15)	242.33(3)
Z	2	2	2
crystal color	colorless	colorless	colorless
crystal size, mm	0.055 × 0.055 × 0.09	0.041 × 0.052 × 0.058	0.037 × 0.047 × 0.092
ρ_{calc}, g cm^{-3}	6.259	6.257	6.226
μ, mm^{-1}	14.997	14.993	14.919
θ_{max}, deg	72.67	72.644	73.222
reflections collected	3367	3815	4015
R_{int}	0.0513	0.0497	0.0895
unique reflections	615	619	633
parameters refined	32	32	32
R_1, wR_2 [Fo > 4 sig(Fo)]	0.0206, 0.0547	0.0194, 0.0508	0.0314, 0.0756
goodness-of-fit	1.134	1.055	0.961
diff. peak and hole, e Å^{-3}	1.88, −2.59	0.9, −1.96	2.23/−1.81

tetrahedral coordination, which also results in a structure consistent with the Li-filled rutile-related framework motif. The chains in LIAO are composed of edge-sharing octahedra, with a chain width that alternates between one and two octahedral groups. To the best of the authors' knowledge, this is the first example of a rutile-related phase with this chain structure, which is remarkable given the chemical and structural diversity within the rutile-related family. A search of the inorganic crystal structure database reveals more than 60 phases with the $FeTa_2O_6$ (trirutile) structure type alone, a subfamily of rutile which has a 2:1 cation ordering in its chains, just like the framework in LIAO, but formed of simpler chains of fixed width.[1,23,24] As such, LIAO represents a potential new dimension for material discovery in this structural family. With further study, the frequency and variation of width changes in edge-sharing chains may function as new design parameters with which the properties of target materials are tuned, in both theoretical and experimental studies. Here, several properties of LIAO are characterized, providing some insights into LIAO and the effect of its unique tunnel structure on ionic mobility.

EXPERIMENTAL SECTION

Synthesis. Powder samples of LIAO were synthesized using standard solid-state techniques. Stoichiometric amounts of Li_2CO_3 (Aldrich, 99.999%), In_2O_3 (Alfa Aesar, 99.994%), and Sb_2O_3 (Aldrich, 99%) were ground together with acetone using a mortar and pestle until homogenous. The mixtures were then heated in air in a platinum crucible with an alumina lid to 1173 K at 5 K/min and held for 8 h to allow for the decomposition of Li_2CO_3 and ensure oxidation of Sb^{3+} to Sb^{5+}.[25] After cooling to room temperature at 5 K/min, the samples were rehomogenized using a mortar and pestle and then pressed into 13 mm-diameter cylindrical pellets. The pellets were returned to their crucibles and reacted at 1473 K for 20 h with the same heating and cooling rates as in the prereaction. White sintered pellets were obtained. Single crystals of LIAO were grown using a Li_2MoO_4 flux. Polycrystalline LIAO was combined with Li_2MoO_4 in a 1:10 ratio by weight. The mixture was heated in a capped platinum crucible in air to 1523 K at 5 K/min. After 16 h, the furnace was cooled to 1223 K at 3 K/h and then returned to room temperature at 5 K/min. The solidified product was sonicated in 200 mL of water and then vacuum-filtered. A mixture of yellow, rod-like crystals of $Li_3InMo_3O_{12}$ and clear, well-faceted crystals without a well-defined shape, identified as LIAO, was obtained.

Structural Characterization. Phase identity and purity were investigated using laboratory powder X-ray diffraction (PXRD) patterns collected over a 2θ range of 10−60° on a Rigaku IV (Ultima) X-ray diffractometer with Cu Kα (λ = 1.54 Å) radiation under ambient conditions. Single-crystal XRD was used to determine the structure of LIAO at 100, 323, and 500 K. To ensure reproducibility of the structure, a new crystal was used for each collection. Crystallographic data are reported in Table 1. CIFs are available for download in the Supporting Information and using CSD codes 1976009−1976011. Single-crystal diffraction data were collected at 100, 323, and 500 K using a Bruker Apex II CCD diffractometer with monochromated Mo Kα (λ = 0.71073 Å) radiation. The crystal-to-detector distance was 40 mm. SAINT V8.38A was used for data integration, and a multiscan absorption correction was applied using SADABS.[26,27] The structure was solved using SHELXS and refined using SHELXL.[28,29] No additional symmetry was found when checking for higher symmetry using PLATON.[30] High-temperature PXRD data were collected at 50 K intervals between 300 and 1200 K on a STOE-STADI-MP powder diffractometer equipped with an asymmetric curved germanium monochromator (Mo Kα_1 radiation, λ = 0.70930 Å) and one-dimensional silicon strip detector (MYTHEN2 1K from DECTRIS). The line-focused Mo X-ray tube was operated at 50 kV and 40 mA. The powder was packed in a 0.3 mm quartz capillary and placed into the furnace. Temperature stability is typically 0.1 K. Intensity data from 0 to 45° 2θ were collected over a period of 45 min. Instrumental shifts and peak shape were calibrated against an NIST silicon standard (640d) prior to the measurement. Powder diffraction data were analyzed by Rietveld refinement using the General Structure Analysis System II (GSAS II) package.[31]

Solid-State Nuclear Magnetic Resonance Spectroscopy. ^{6}Li (I = 1) and ^{7}Li (I = 3/2) solid-state nuclear magnetic resonance (NMR) spectra were recorded in a static magnetic field of 9.4 T with a Bruker AVANCE III spectrometer. The samples, LIAO and $LiSbO_3$, were separately packed into 4.0 mm-diameter zirconia rotors, and spectra were recorded under static and 5 and 12.5 kHz magic-angle spinning (MAS) conditions using a Bruker narrow bore 4.0 mm HX probe. T_1 (spin−lattice) relaxation was measured with a saturation

https://dx.doi.org/10.1021/acs.chemmater.0c01491
Chem. Mater. 2020, 32, 4785−4794

recovery pulse. Quantitative ^{6}Li spectra were measured with a single 90° radio frequency (rf) pulse of 1.6 μs; the recycle delay was fixed at 200 s for LIAO and at 100 s for $LiSbO_3$, approximately 5 × T_1. ^{6}Li enrichment was unnecessary owing to the relatively large sample volume. ^{7}Li spectra were measured with a single <90° rf pulse to ensure sufficient quadrupolar excitation; a liquid 90° pulse of 4.0 μs was calibrated on 1.0 M $LiCl_{(aq.)}$, and a 2.5 μs pulse was applied to the solids. For each measurement, 8 or 16 scans were coadded. A recycle delay of 10 s was used for the ^{7}Li spectra. All $^{6/7}$Li spectra were referenced to the primary standard 1.0 M $LiCl_{(aq.)}$ at 0 ppm. Density functional theory (DFT) was used to compute the chemical shift tensor and quadrupolar tensor of LIAO and $LiSbO_3$. The calculations were performed in the plane wave code CASTEP v19.11 with "on-the-fly" ultrasoft pseudopotentials and the general-gradient-approximation Perdew–Burke–Ernzerhof exchange-correlation functional.[32−34] The plane-wave basis set was truncated at an energy cutoff of 700 eV, and integration over reciprocal space was performed using 7 × 7 × 4 and 7 × 4 × 7 Monkhorst–Pack grids for LIAO and $LiSbO_3$, respectively.[35] Structures were geometry-optimized prior to NMR calculations.[36−38] Spectral simulations of the calculated tensors were performed with the solid lineshape analysis (SOLA) interface in TopSpin v3.6.1. Euler angles relating the orientation of magnetic shielding to the electric field gradient (EFG) tensors were generated in MagresView v1.6.2.[39] The isotropic shift δ_{iso} is defined in the Haeberlen convention $\delta_{iso} = \frac{\delta_{XX} + \delta_{YY} + \delta_{ZZ}}{3}$ with the chemical shift anisotropy (CSA) defined as CSA = $\delta_{ZZ} - \delta_{iso}$ and the shift asymmetry η_{CSA} defined as $\eta_{CSA} = \frac{\delta_{YY} - \delta_{XX}}{\delta_{ZZ} - \delta_{iso}}$. With these definitions, the principal components of the shift tensor are ordered such that $|\delta_{ZZ} - \delta_{iso}| \geq |\delta_{XX} - \delta_{iso}| \geq |\delta_{YY} - \delta_{iso}|$. The abovementioned definition of CSA is sometimes referred to as the reduced anisotropy, which is equal to 2/3 of the "full" anisotropy $\delta_{ZZ} - \frac{\delta_{XX} + \delta_{YY}}{2}$ used by some authors and programs. The quadrupolar coupling constant C_Q is defined by the nuclear quadrupole moment (Q) and the largest principal component V_{ZZ} of the EFG at the nucleus according to $C_Q = \frac{eQV_{ZZ}}{h}$, where e is the electric charge and h is Planck's constant. The quadrupolar asymmetry parameter η_Q is defined using the EFG tensor components as $\eta_Q = \frac{V_{XX} - V_{YY}}{V_{ZZ}}$, with components similarly ordered such that $|V_{ZZ}| \geq |V_{YY}| \geq |V_{XX}|$.

Optical Characterization. Diffuse reflectance measurements were performed on a sintered pellet sample of LIAO using a Lambda 1050 UV–vis spectrophotometer with integrating sphere attachment (PerkinElmer). Background spectra were collected on compacted polystyrene. The Kubelka–Munk transformation was used to transform the collected spectra into pseudo-absorbance as a function of energy.[40] Linear extrapolations were performed on both the band edge and the background immediately preceding it, and the intersection was taken as an estimate for the optical band gap for each sample. Powder second harmonic generation (SHG) measurements were performed using a pulsed Nd:YAG laser (Quantel Laser, Ultra 50) with a wavelength of 1064 nm. The sample was loaded into a fused silica tube and placed on the sample holder. The generated SHG signal was separated from the fundamental light using a 1064 nm filter, detected using a photomultiplier tube, and shown on an oscilloscope (Tektronix, TDS3032). For comparison, α-SiO_2 (polycrystalline powder) was measured under the same conditions.

Impedance Spectroscopy. Polycrystalline compacts of LIAO were prepared from powders synthesized using the solid-state reaction methods described above. The resulting powders were ground further with agate media in a Fritsch pulverisette 7 ball mill for 12 cycles of 5 min at 500 rpm. The ball-milled powders were then mixed in ethanol with 2% polyvinyl butyral by weight and a small amount of dibutyl phthalate as binding and plasticizer agents. Then, the sample was pressed into a thin, dense pellet first in a uniaxial press and then in an isostatic press at 250 MPa for 20 min. The pellet was subsequently heated at 3 K/min to 573, 773, and 1373 K and held for 3 h at each temperature to burn out organics and sinter to 68% of theoretical density. The pellet was phase-pure, as confirmed by XRD. Pt electrodes were applied as a paste and fired at 1173 K for 1 h (Au electrodes on a second sample produced nearly identical results). Impedance spectroscopy measurements were performed on the prepared pellet in a custom test station using a Faraday cage-incased sample holder and a Modulab XM (Solartron Analytical) analyzer equipped with an XM Femto Ampere card.[41] Under flowing (40 sccm) synthetic air, the sample was heated from room temperature to 873 K in 25 K increments and held for 30 min before each impedance measurement from 1 MHz to 1 Hz at a perturbation voltage of 20–50 mV.

RESULTS AND DISCUSSION

Structural Description. Initial structural solutions were carried out with body centering as recommended by XPREP, the space group determination program of the ShelXTL package. Although the obtained structures result in low refinement parameters (R_1 = 1.66% and wR_2 = 4.04%), they also exhibit several unrealistic features, including half-filled O positions and nonpositive definite atoms (see Figure S1). Repeating the measurement at higher temperature (323 K) eliminates the nonpositive definite atoms but otherwise gives the same structural solution, suggesting that the unrealistic solution was not caused by freezing of disorder at low temperatures. Comparison of the predicted powder pattern for this structure with experimental patterns on the material revealed several unaccounted-for peaks corresponding to the (120), (113), and (212) reflections for the given lattice parameters, all of which should be absent with a body-centered space group. As such, the crystal structure was solved with primitive centering. The resulting solution, summarized in Tables 1 and 2 with atomic arrangement depicted in Figures 1a and S2, retains the same metric unit cell as the body-centered structure but displays several improvements; it has no nonpositive definite atoms and only half the number of O

Table 2. Atomic Coordinates in LIAO at 100 K[a]

atom	Wyckoff position	x	y	z	U_{eq}[b]
In	4f	0.5	0	0.30098(2)	2.32(9)
Sb	2a	0.5	0.5	0.5	2.03(9)
Li	4g	0.051(2)	0.107(3)	0.5	10(2)
O1	8h	0.2785(3)	0.3368(3)	0.34348(15)	8.5(3)
O2	4g	0.6984(4)	0.1837(4)	0.5	3.9(3)

[a]For 323 and 500 K, see Table S2. [b]For full anisotropic displacement parameters, see Supporting Information CIFs.

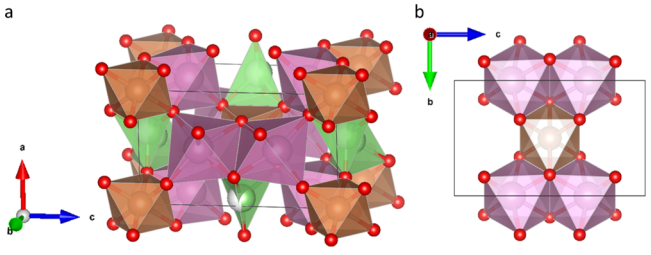

Figure 1. Structural Refinement of LIAO. (a) Single-crystal solution as viewed down the [281] direction. (b) Portion of an isolated edge-sharing chain of InO_6 and SbO_6 octahedra contained within a single unit cell, viewed down the a-axis. Purple, orange, and green polyhedra are respectively centered on the 4f (In^{3+}), 2a (Sb^{5+}), and 4g (Li^{+}) crystallographic sites. Red spheres are O^{2-} ions.

https://dx.doi.org/10.1021/acs.chemmater.0c01491
Chem. Mater. 2020, 32, 4785−4794

positions, all of which are fully occupied. Notably, the predicted powder pattern for the primitive solution accounts for all the peaks in the experimental one. A Rietveld refinement performed with this structure is shown below in Figure 2 with relevant parameters summarized in Table S1.

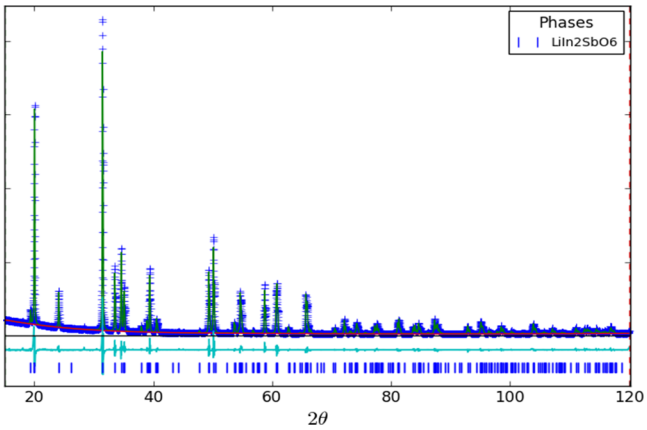

Figure 2. Rietveld refinements of powder LIAO samples. (Blue crosses) Observed powder pattern. (Green) Predicted pattern. (Red) Background. (Light Blue) Difference pattern. (Blue ticks) Predicted reflections from LIAO. *R*-Factors from the fit are 6.22% (R_p) and 8.88% (R_{wp}).

The crystal structure of LIAO may be described as a distorted hexagonal close-packed array of O^{2-} ions with half the octahedral holes filled with In^{3+} and Sb^{5+} and one-sixth of the tetrahedral holes containing Li^+. The InO_6 and SbO_6 octahedra make up a framework of edge-sharing chains along the *b* axis connected to each other via corner sharing, with Li^+ distributed within channels between them. Along the length of the chains, dimers of InO_6 octahedra alternate with single SbO_6 octahedra, and thus, the width of the chain along the *c* direction varies between one and two octahedra for each step in the *b* direction, as shown in Figure 1b. This motif is known as a "diamond chain" in magnetic materials with analogous dimer−monomer−dimer arrangements of unpaired spins.[42,43] Table 3 presents selected bond lengths and angles for LIAO at 100 K (for 323 and 500 K, see Table S3). While the Sb−O bond lengths are very close in value, producing only a slight axial elongation in SbO_6 octahedra, the In−O bond length variation indicates a much more significant distortion. The differences in distortion are also evident in the O−M−O octahedral angles, which are close in value in SbO_6 but vary significantly in InO_6. The In^{3+} in these InO_6 octahedra are shifted away from the center of the dimer toward the opposite edge, likely owing to electrostatic repulsion between the two cations arising from the asymmetric edge sharing surrounding the dimers. This effect is well known in other rutile-related phases with doubled octahedral chains and is distinct from displacements along the chain in rutile-related NbO_2 and VO_2, in which metal−metal bond formation causes the cations in adjacent dimers to move away from each other.[4,44] In^{3+} does not have the d^1 configuration which makes the latter favorable, and the In^{3+} centers which "approach" each other remain separated by over 5 Å owing to the intervening channel and therefore cannot be participating in metallic bonding. Complete ordering of In and Sb within these chains is supported by bond valence calculations, as shown in Table S4. The chains are arranged in a checker-board fashion when viewed down the *b*-axis with each being diagonally connected to four others. Connected chains are staggered along *b* such that Sb-centered octahedra exclusively share corners with InO_6 dimers and vice versa. The spaces between chains formed by this arrangement are the channels in which the Li^+ tetrahedra are located. These channels have the same alternating structure as the chains.

Table 3. Selected M−O Bond Lengths, O−M−O Bond Angles, and Multiplicities in LIAO (100 K)

bond lengths (Å)		angles (°)	
2× In−O1	2.1537(17)	1× O1−In−O1	104.72(6)
2× In−O1	2.1009(15)	2× O1−In−O1	96.59(6)
2× In−O2	2.2592(13)	2× O1−In−O1	95.70(6)
		2× O1−In−O2	89.80(4)
		2× O1−In−O2	89.46(4)
		1× O2−In−O2	77.04(1)
		2× O1−In−O2	74.65(4)
4× Sb−O1	1.9903(15)	4× O2−Sb−O1	94.83(5)
2× Sb−O2	1.966(2)	2× O1−Sb−O1	91.39(6)
		2× O1−Sb−O1	88.61(6)
		4× O2−Sb−O1	85.17(5)
2× Li−O1	2.185(11)	1× O2−Li−O2	142.3(6)
1× Li−O2	1.841(11)	2× O2−Li−O1	113.08(4)
1× Li−O2	2.008(14)	2× O2−Li−O1	95.53(4)
		1× O1−Li−O1	79.01(6)

The Li^+ ions reside, at 50% occupancy levels, in tetrahedral sites sandwiched between InO_6 dimers. The coordination polyhedra defined by these sites are somewhat distorted, as indicated by the bond lengths in Table 3, but these distances remain within 1.8−2.2 Å, the normal range for LiO_4 tetrahedra. Solid-state NMR spectroscopy provides confirmation of Li coordination. The ^{6}Li central resonances and ^{7}Li full spinning sideband manifolds of LIAO and $LiSbO_3$ at 5 kHz MAS are shown in Figure 3; ^{7}Li central peaks at 5 kHz are given in Figure S3 along with an analysis of line widths. The spectra show the Li resonance in LIAO to occur at 0.65(1) ppm, whereas that in octahedral LiO_6 in $LiSbO_3$ to occur at −0.05(2) ppm. These shifts are typical for LiO_4 and LiO_6, respectively.[45] As Li has a small chemical shift range, coordination was also probed by examining the simulated and experimental quadrupolar parameters, which are very sensitive to local coordination symmetry and distortions. Simulations of the spectra were performed using the X-ray single-crystal structure solution described in this work for LIAO and the known *Pncn* structure of $LiSbO_3$ (ICSD39574), whereas experimental parameters were obtained by fitting the quadrupolar line shapes of the ^{7}Li MAS NMR spectra. As depicted in Figure 3b and quantified in Table 4, the experimental data for LIAO are in good agreement with the tetrahedral lithium site calculated in the *Pnnm* structure. Thus, the occupancy of Li in tetrahedral sites is fully established. Notably, the distance between Li sites in LIAO is significantly smaller than the typical separation of tetrahedrally coordinated Li (3 Å), suggesting that there may be a low barrier to migration between them.[18] Moreover, the arrangement is reminiscent of that of Li in the paraelectric phases of known ferroelectrics $LiNbO_3$ and $LiTaO_3$.[46,47] However, no change to a lower symmetry space group is observed in the single-crystal solution LIAO between 500 and 100 K, in contrast to the

https://dx.doi.org/10.1021/acs.chemmater.0c01491
Chem. Mater. 2020, 32, 4785−4794

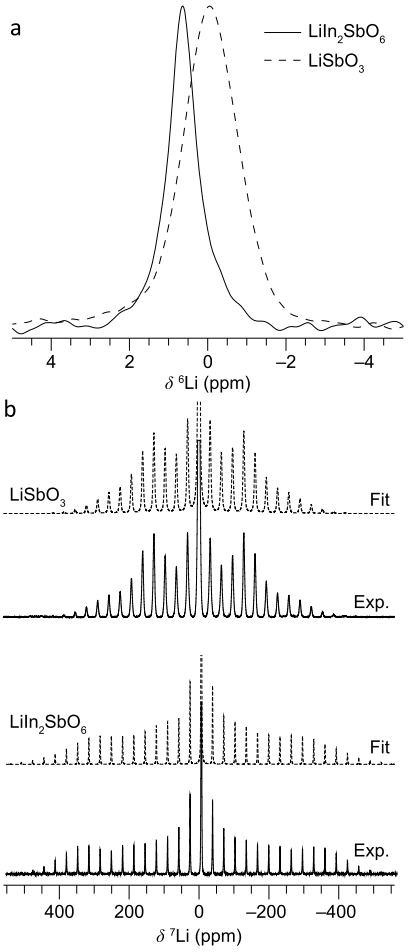

Figure 3. $^{6/7}$Li solid-state 5 kHz MAS NMR spectroscopy. (a) ^{6}Li central resonance and (b) ^{7}Li spectra showing the spinning sidebands and fits to the experimental line shapes. Fit parameters are given in Table 4.

Table 4. Calculated and Experimental NMR Parameters of LIAO and $LiSbO_3$

	LIAO		$LiSbO_3$	
parameter	calculated	experimental fit	calculated	experimental fit
isotropic shift (δ_{iso}; ppm)	0.65[a]	0.65(1)	−0.55[a]	−0.05(2)
chemical shift anisotropy (CSA; ppm)	−7.3	n/a[b]	−2.8	n/a[b]
shift asymmetry (η_{CS})	0.13	n/a[b]	0.18	n/a[b]
quadrupolar coupling (C_Q; kHz)	141	150(10)	103	108(5)
quadrupolar asymmetry (η_Q)	0.57	0.6(1)	0.42	0.2(1)
Euler angles (α, β, γ; °)	−90, 10.4, 90	n/a[b]	0, 168.3, 90	n/a[b]

[a]Calculated shielding values must be referenced. Here, the shielding of LIAO was arbitrarily converted to the experimental shift value, which allows for relative comparison of the LIAO and $LiSbO_3$ shifts. [b]Too small to significantly affect the fit. Calculated values used directly without refinement.

observed Li ordering which accompanies the ferroelectric transition in $LiNbO_3$ and $LiTaO_3$.

Relationship to Known Structures. The original report of LIAO by Tarte and Gabelica-Robert noted clear relationships between LIAO and $LiSbO_3$.[20] The compounds have the same cation−anion ratio and share three out of four elemental components. The reported PXRD patterns are analogous except for the (110) reflection, which is forbidden in $LiSbO_3$ and observed for LIAO. From these similarities, the authors hypothesized that the LIAO structure was identical to that of $LiSbO_3$ with cation ordering that reduced the symmetry from *Pnna* to *Pnn*2. However, the true structural relationship between the phases, as determined here, is more complex. The relationship is most easily understood by looking at a single set of AB layers in the hexagonal close-packed anion array for each phase, with cation positions indicated.[48] Figure 4 shows how $LiSbO_3$ can be transformed to LIAO in two steps: (1) replacing every other adjacent set of octahedrally placed Li^+/Sb^{5+} ions with a pair of In^{3+} ions and (2) splitting the remaining Li^+ content between the two nearest, equidistant tetrahedral positions. It should be noted that the hypothetical structure produced after step 1 exhibits the *Pnn*2 symmetry expected by Tarte and Gabelica-Robert. The second step produces mirror plane symmetry between the chains, resulting in our observed *Pnnm* space group. Second harmonic generation, which is only observed from space groups lacking inversion symmetry such as *Pnn*2, is not detected in LIAO.

The adoption of tetrahedral coordination by Li^+ transforms the 3D edge-sharing octahedral network of $LiSbO_3$ into the filled framework arrangement, described above, with the connectivity of a Li-filled rutile-related phase. However, the framework of LIAO is distinguished from other members of the rutile-related family by the alternating width along its chains and the ordering of cations within them. Isolated chains from several representative rutile-like structure materials are compared in Figure 5a. The prototype rutile has chains that are 1 × 1, meaning that each octahedral unit shares edges only with the octahedra ahead of and behind it in the direction of the chain. The related ramsdellite structure has 2 × 1 chains. The diamond pattern of LIAO chains can be thought of as a one-to-one alternation of these two chain structures along the chain direction. In fact, intergrowths of rutile and ramsdellite containing both types of chains have been reported previously, such as in γ-MnO_2 or $Li_{0.9}Ti_{2.94}O_6$.[4,5,13,49] The TiO_6 framework of the latter material, shown in Figure 5b, even has a one-to-one ratio of rutile and ramsdellite, as found in the LIAO framework. However, the slabs of rutile and ramsdellite alternate in a direction perpendicular to the chains rather than parallel to them (as in LIAO), thereby preserving the fixed width of any individual chain. To the best of the authors' knowledge, this is true for all reported intergrowths of these two structures. Thus, the chains of LIAO appear unique in this aspect.

As a consequence of the unique pattern of LIAO chains, their orientation with respect to the rows of O in the close-packed layer is rotated by 30° as compared to similar structures (Figure 6). According to Baur, members of the rutile-related family are sometimes referred to as "3 Å structures" because, in oxides and fluorides, the lattice parameter parallel to the chain direction is either ∼3 Å or a multiple of that in ordered variants such as trirutile.[1] The corresponding value in LIAO (5.33 Å) deviates but still bears a close geometrical relationship to the characteristic length, as shown in Figure 6.

An explanation for the formation of alternating-width chains instead of either rutile or ramsdellite ones deserves some

https://dx.doi.org/10.1021/acs.chemmater.0c01491
Chem. Mater. 2020, 32, 4785−4794

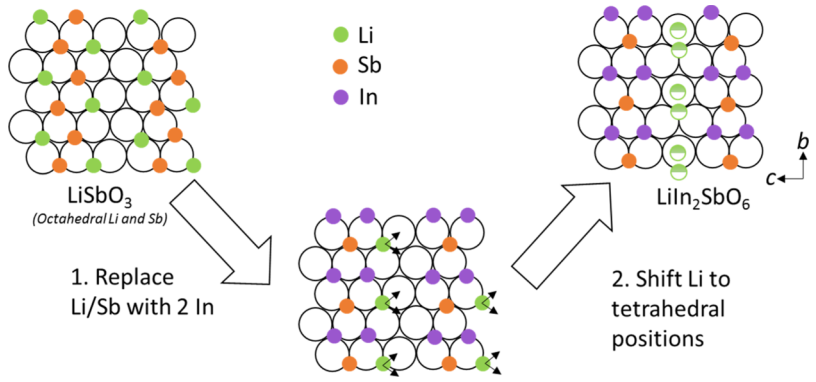

Figure 4. Relationship between the close-packed layers of $LiSbO_3$ and LIAO. Open circles are O^{2-} ions. Cation positions for all framework ions of LIAO are present in $LiSbO_3$, and Li positions are slightly offset between tetrahedral and octahedral sites.

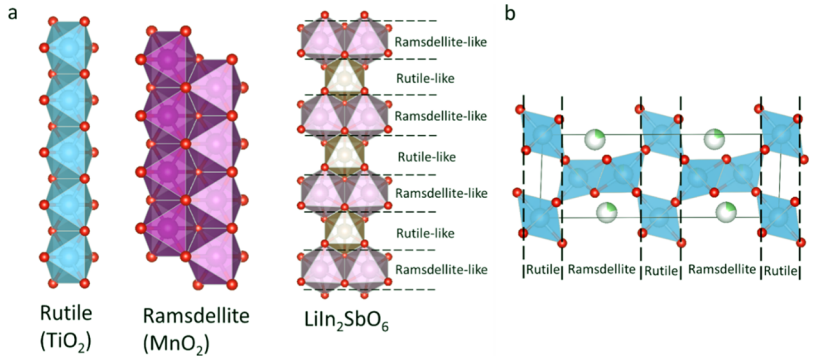

Figure 5. (a) Several-unit-cell long segment of an isolated chain from selected rutile-like phases viewed perpendicular to the chain direction.[1−7] Regions of LIAO chains are labeled with the structure they most closely resemble. (b) Intergrowth structure of rutile and ramsdellite (1:1) as observed in Li-intercalated ramsdellite $Li_{0.9}Ti_{2.94}O_6$ viewed parallel to the chain direction, with rutile and ramsdellite slabs indicated.[7]

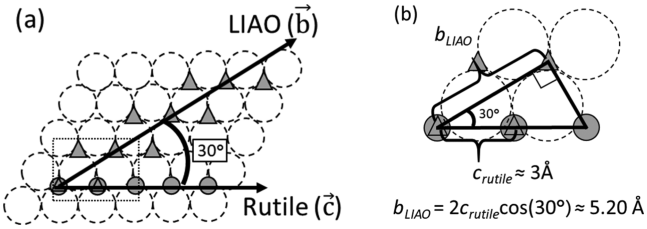

Figure 6. Geometrical relationship between occupied octahedral holes in a single, ideal close-packed layer (dashed circles) in the LIAO (triangles) and rutile (circles) structures. (a) Rutile octahedral sites lie parallel to the rows of close-packed O^{2-} ions, whereas LIAO chains are rotated by 30°. (b) Close-up of the boxed region in (a). The observed chain direction lattice parameters in LIAO (5.33 Å) arise from a characteristic value of ∼3 Å in rutile-related oxides.

consideration. The characteristics of the framework in LIAO alone are unlikely to account for the formation of its unique chain structure. Neither its cation chemistry nor its stoichiometry is unique among the rutile-related phases. For example, $InSbO_4$ crystallizes with a random rutile structure rather than an ordered variant, indicating that In^{3+} and Sb^{5+} are similar enough that they do not necessarily favor ordering in related materials.[50,51] Likewise, many compounds with the trirutile structure, such as $ZnSb_2O_6$, have the $M'M''_2O_6$ stoichiometry of the In_2SbO_6 framework in LIAO. These phases demonstrate that the 1 × 1 chains of rutile can readily accommodate ordering commensurate with the 1:2:6 stoichiometry.[1] Most importantly, unlike other rutile-related phases with Li in the channels, attaining charge neutrality in the structure requires incorporation of Li^+ into the framework of LIAO as In^{3+} and Sb^{5+} cannot be further oxidized to compensate for empty channel sites. Thus, the presence of Li appears critical to the formation of alternating-width chains.

Li^+ behavior in Li-filled TiO_2 provides insight into how this hypothesis could be true. In the 2 × 1 channels of the ramsdellite-type TiO_2, electrochemical insertion of up to 0.5 Li per framework cation site is found to favor tetrahedral sites owing to space and charge screening considerations.[16,18,19] With 0.33 Li per framework site, tetrahedral Li coordination in LIAO is likely a result of the same considerations. Furthermore, the intergrowth phase shown in Figure 5b, formed by high-temperature solid-state methods, suggests that under certain conditions, such as high temperatures or reducing environments, Li^+ coordinated by 2 × 1 chains in tetrahedral sites is found in the thermodynamic ground state.[13] Likewise, DFT and potential modeling studies have found a reversal in the relative stability of the rutile and ramsdellite-type polymorphs of Li_xTiO_2 with increasing x, such that 2 × 1 chains are favored over 1 × 1 at higher Li^+ content.[12,18] Thus, the presence of Li provides a thermodynamic driving force for the formation of 2 × 1 units in the chain. The alternating chain structure of LIAO appears to be another mechanism to provide Li^+ with this favorable coordination environment without a fully 2 × 1 chain. It is possible that ramsdellite-type chains are destabilized for LIAO relative to the alternating-width chains by increased repulsion from highly charged Sb^{5+} centers being in closer proximity to each other or Li^+. This is consistent with the fact that In^{3+} and Sb^{5+} are fully ordered in LIAO such that the distance between Li^+ and Sb^{5+} is maximized, despite the

https://dx.doi.org/10.1021/acs.chemmater.0c01491
Chem. Mater. 2020, 32, 4785−4794

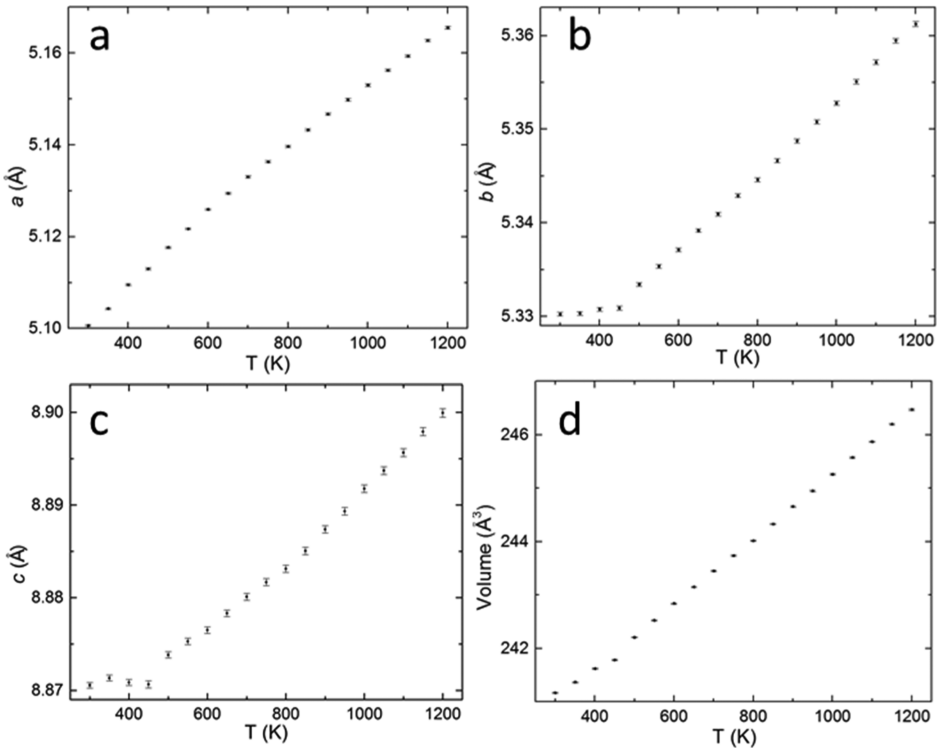

Figure 7. Unit cell lattice parameters *a*, *b*, and *c* (a–c) and volume (d) as a function of temperature determined by refinement of high-temperature PXRD data.

same two cations showing full disorder in rutile-type $InSbO_4$ (no Li present).[50] As such, the other stoichiometrically analogous phases identified by Tarte and Gabelica-Robert as having cation-ordered $LiSbO_3$ structures (LiM_2SbO_6, M = Sc, Mn, and Fe) may also exhibit these alternating-width chains.[20]

Thermal Behavior. The refined unit cell volume and lattice parameters as a function of temperature up to 1200 K are depicted in Figure 7. The overall volume expands nearly linearly over the entire temperature range, with a slight anomaly at 450 K (Figure 7d). Examination of the individual lattice parameter behaviors shows that this expansion is dominated by the behavior in the *a* direction, which shows only a very slight change at 450 K. Expansion along *b* and *c* is more than an order of magnitude smaller than that along *a* at ambient temperature and increases substantially on heating at 450 K. These distinct changes suggest the possibility of a phase transition. However, the evolution of the PXRD pattern over the measured temperature range (Figure S4) shows no apparent changes in the peaks other than shifts in their positions, suggesting the absence of structural changes involving symmetry changes or a decomposition reaction. Furthermore, single-crystal XRD performed at 500 K (Figure S2) gives an identical solution to those at 100 and 323 K, accounting for thermal expansion and larger atomic displacement parameters expected at higher temperatures. Thus, although the origin of the slope change in the refined *b* and *c* parameters is unclear, LIAO appears to be stable up to 1200 K, consistent with previous reports of significant thermal stability in related materials.[22]

Property Characterization. The pseudo-absorbance ($F(R)$) spectra of LIAO were extracted from diffuse reflectance data. Plots of the data for LIAO to the powers of 1/2 and 2, depicted in Figure 8, show that the energy dependence appears linear only in the latter case, as is expected for a direct band

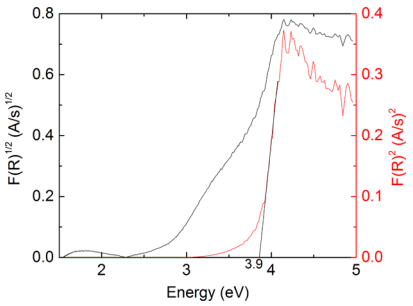

Figure 8. Comparison of $F(R)^{1/2}$ and $F(R)^2$ extracted from diffuse reflectance measurements of LIAO. Extrapolation of the linear portion of $F(R)^2$ suggests a direct band gap of 3.9 eV.

gap material.[32] Extrapolation of this curve to the *x*-axis gives an estimated band gap of 3.9 eV, consistent with the band gaps of chemically related phases such as $LiInO_2$.[52]

The large band gap of LIAO likely precludes significant electronic conductivity in the pure phase. As expected, measurements with a four-point probe indicated an immeasurably large sheet resistance. However, the channels in the LIAO structure and the split occupancy and tetrahedral coordination of Li^+ are conditions which have been considered favorable to ionic conductivity in related materials.[8,14−18] Li^+ conductors that are electronically insulating are of interest as solid-state electrolytes, motivating the AC impedance measurements.[53] Room temperature impedance spectra, Figure 8a, indicate that LIAO is not a good Li^+ conductor, despite the favorable structural features. Under ambient conditions, LIAO has a moderate resistance that rapidly increases as dry gas is introduced. The behavior suggests that under ambient humidity conditions, transport in LIAO is dominated by H^+/H_3O^+ migration along grain boundaries or internal pore

https://dx.doi.org/10.1021/acs.chemmater.0c01491
Chem. Mater. 2020, 32, 4785−4794

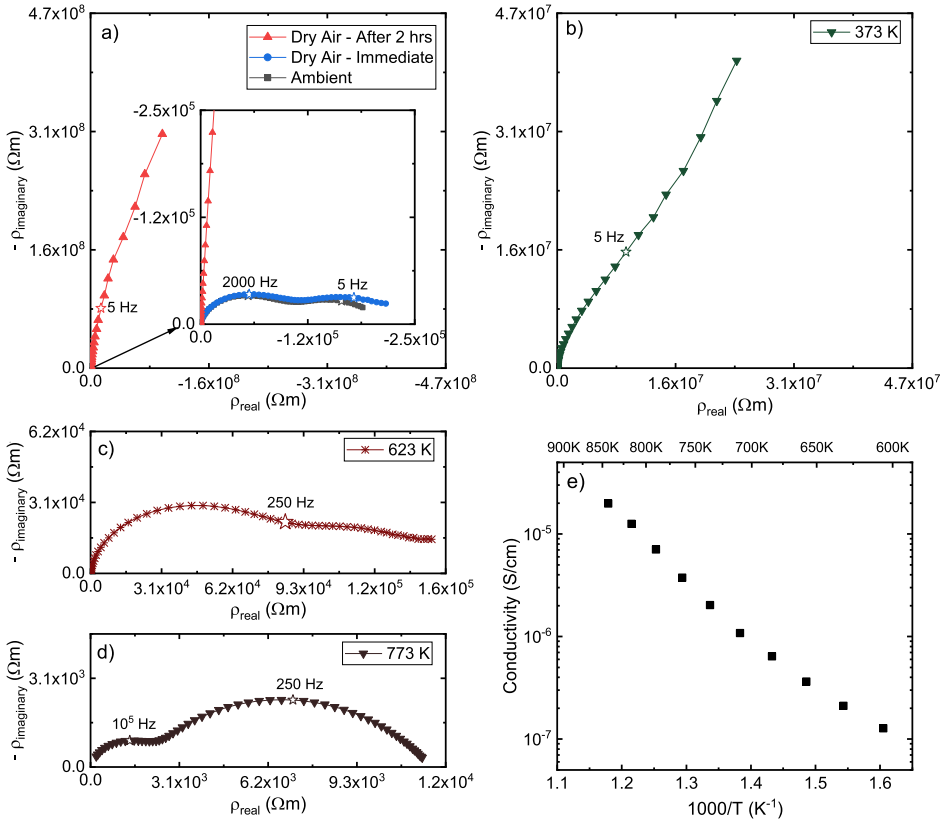

Figure 9. Impedance spectra of LIAO at (a) room temperature, (b) 373, (c) 623, and (d) 773 K, and (e) bulk conductivity. Room temperature spectra are measured under ambient conditions (blue), immediately under synthetic air (red) and after drying in synthetic air for 2 h (blue). High-temperature spectra are measured under synthetic air. Select frequencies are indicated by a star. Bulk conductivity values are those corresponding to the high frequency arc spectra such as in (c,d).

surfaces and changes to bulk sluggish Li^+ conduction under dry conditions. On heating (select spectra in Figure 9b–d and a complete data set in Figure S5), the overall resistance of the sample decreases as reflected in the decreasing magnitude of the impedance arcs. At temperatures of 623 K and above, the spectra are characterized by two arcs, typical of polycrystalline, in which the high frequency arc reflects bulk transport and the low frequency arc reflects transport across resistive grain boundaries. The bulk conductivity obtained by such an interpretation and associated impedance fitting, Figure 9e, reveals a conductivity, σ, of 1.3×10^{-7} S/cm at 623 K and an activation energy for transport, E_σ, of 1.1 eV (taking the conductivity to be of the form $\sigma = \frac{A}{T}\exp\left(\frac{-E_\sigma}{k_b T}\right)$, where A is a constant, T is temperature, and k_b is Boltzmann's constant). The relative dielectric constant obtained from the analysis is ~70, a reasonable value for an oxide material far from any phase transitions.[54] Although the large band gap suggests that the transport is ionic, it is not possible to rule out a possible electronic contribution to the conductivity on the basis of the features of the impedance spectra.

CONCLUSIONS

The previously unknown structure of LIAO was solved and features a unique Li-filled rutile-related framework structure. The framework is built from chains of edge-linked polyhedra, with widths that alternate along the chain length between one (rutile-like) and two (ramsdellite-like) polyhedra. High temperature PXRD reveals thermal stability up to 1200 K. AC impedance reveals a moderate to poor conductivity, with an activation energy for charge transport of 1.1 eV. Investigation of other phases previously believed to be isostructural to LIAO, such as $LiSc_2SbO_6$ or $LiFe_2SbO_6$, is expected to reveal more cases of this unique channel structure. Further examples of the LIAO structure type will present an opportunity to decouple the effects of the alternating-width chains from that of the framework chemistry (which is not readily oxidized or reduced in LIAO) on the observed ionic conduction behavior and potentially make chain width oscillation a new design parameter for inorganic framework oxides.

ASSOCIATED CONTENT

Supporting Information

The Supporting Information is available free of charge at https://pubs.acs.org/doi/10.1021/acs.chemmater.0c01491.

Crystallographic Data for LIAO 1976009 (CIF)
Crystallographic Data for LIAO 1976010 (CIF)
Crystallographic Data for LIAO 1976011 (CIF)
Crystal structures and powder patterns of nonphysical body-centered structural solutions for LIAO; single-crystal structures of LIAO at 323 and 500 K; Rietveld refinement parameters for LIAO; atomic coordinates in LIAO at 323 and 500 K; selected M–O bond lengths, O–M–O bond angles, and multiplicities in LIAO at 323 and 500 K; bond valence analysis in LIAO at 100 K; ^{7}Li NMR spectra of the central resonance of LIAO and $LiSbO_3$; temperature-dependent PXRD pattern of LIAO

https://dx.doi.org/10.1021/acs.chemmater.0c01491
Chem. Mater. 2020, 32, 4785–4794

from 300 to 1200 K; and temperature-dependent impedance spectra of LIAO (PDF)

AUTHOR INFORMATION

Corresponding Author

Kenneth R. Poeppelmeier − *Department of Chemistry, Northwestern University, Evanston, Illinois 60208, United States;* orcid.org/0000-0003-1655-9127; Email: krp@northwestern.edu

Authors

Steven Flynn − *Department of Chemistry, Northwestern University, Evanston, Illinois 60208, United States*

Sheel Sanghvi − *Department of Materials Science and Engineering, Northwestern University, Evanston, Illinois 60208, United States;* orcid.org/0000-0002-9962-3587

Matthew L. Nisbet − *Department of Chemistry, Northwestern University, Evanston, Illinois 60208, United States;* orcid.org/0000-0001-9531-9193

Kent J. Griffith − *Department of Chemistry, Northwestern University, Evanston, Illinois 60208, United States;* orcid.org/0000-0002-8096-906X

Weiguo Zhang − *Department of Chemistry, University of Houston, Houston, Texas 77204, United States*

P. Shiv Halasyamani − *Department of Chemistry, University of Houston, Houston, Texas 77204, United States;* orcid.org/0000-0003-1787-1040

Sossina M. Haile − *Department of Chemistry and Department of Materials Science and Engineering, Northwestern University, Evanston, Illinois 60208, United States;* orcid.org/0000-0002-5293-6252

Complete contact information is available at: https://pubs.acs.org/10.1021/acs.chemmater.0c01491

Notes

The authors declare no competing financial interest.

ACKNOWLEDGMENTS

The authors would like to thank Christos Malliakas, Zach Mansley, and Charlotte Stern for helpful discussions. This work was supported by the National Science Foundation (DMR-1720139 and DMR-1904701). This work made use of the IMSERC X-ray Facility at Northwestern University, which has received support from the Soft and Hybrid Nanotechnology Experimental (SHyNE) Resource (NSF ECCS-1542205); the State of Illinois and International Institute for Nanotechnology (IIN); and the Jerome B. Cohen X-Ray Diffraction Facility supported by the MRSEC program of the National Science Foundation (DMR-1720139) at the Materials Research Center of Northwestern University and the Soft and Hybrid Nanotechnology Experimental (SHyNE) Resource (NSF ECCS-1542205). Diffuse reflectance was collected at the NU Keck Biophysics Facility. P.S.H. and W.Z. thank the Welch Foundation (Grant E-1457) for support. K.J.G. acknowledges the Joint Center for Energy Storage Research, an Energy Innovation Hub funded by the US Department of Energy, Office of Science, and Basic Energy Sciences.

REFERENCES

(1) Baur, W. H. The Rutile Type and Its Derivatives. *Crystallogr. Rev.* **2007**, *13*, 65−113.

(2) Wells, A. F. *Structural Inorganic Chemistry*, 5th ed.; Oxford University Press, 2012.

(3) Bursill, L. A. Structural Relationships between β-Gallia, Rutile, Hollandite, Psilomelane, Ramsdellite and Gallium Titanate Type Structures. *Acta Crystallogr., Sect. B: Struct. Crystallogr. Cryst. Chem.* **1979**, *35*, 530−538.

(4) Post, J. E.; Heaney, P. J. Neutron and Synchroton X-Ray Diffraction Study of the Structures and Dehydration Behaviors of Ramsdellite and "Groutellite". *Am. Mineral.* **2004**, *89*, 969−975.

(5) Chabre, Y.; Pannetier, J. Structural and Electrochemical Properties of the Proton / γ-MnO_2 System. *Prog. Solid State Chem.* **1995**, *23*, 1−130.

(6) Fujishima, A.; Honda, K. Electrochemical Photolysis of Water at a Semiconductor Electrode. *Nature* **1972**, *238*, 37−38.

(7) Over, H.; Seitsonen, A. P.; Lundgren, E.; Schmid, M.; Varga, P. Direct Imaging of Catalytically Important Processes in the Oxidation of CO over RuO_2(110). *J. Am. Chem. Soc.* **2001**, *123*, 11807−11808.

(8) Soares, A.; Fraisse, B.; Morato, F.; Ionica-Bousquet, C. M.; Monconduit, L. On the Synthesis Conditions for Tailoring Lithium Composition in Ramsdellite Phases: Application for Li-Ion Batteries. *J. Power Sources* **2012**, *208*, 440−446.

(9) Tsuyumoto, I.; Moriguchi, T. Synthesis and Lithium Insertion Properties of Ramsdellite Li_xTiO_2 Anode Materials. *Mater. Res. Bull.* **2015**, *70*, 748−752.

(10) Pérez-Flores, J. C.; Hoelzel, M.; García-Alvarado, F.; Kuhn, A. Structural and Electrochemical Study of Vanadium-Doped TiO_2 Ramsdellite with Superior Lithium Storage Properties for Lithium-Ion Batteries. *ChemPhysChem* **2016**, *17*, 1062−1069.

(11) Yoshikado, S.; Ohachi, T.; Taniguchi, I.; Onoda, Y.; Watanabe, M.; Fujiki, Y. AC Ionic Conductivity of Hollandite Type Compounds from 100 Hz to 37.0 GHz. *Solid State Ionics* **1982**, *7*, 335−344.

(12) Kerisit, S.; Rosso, K. M.; Yang, Z.; Liu, J. Computer Simulation of the Phase Stabilities of Lithiated TiO_2 Polymorphs. *J. Phys. Chem. C* **2010**, *114*, 19096−19107.

(13) Grey, I. E.; Cranswick, L. M. D.; Li, C.; Bursill, L. A.; Peng, J. L. New Phases Formed in the Li−Ti−O System under Reducing Conditions. *J. Solid State Chem.* **1998**, *138*, 74−86.

(14) Koudriachova, M.; Harrison, N. M.; de Leeuw, S. W. Diffusion of Li-Ions in Rutile. An Ab Initio Study. *Solid State Ionics* **2003**, *157*, 35−38.

(15) Murphy, D. W.; Di Salvo, F. J.; Carides, J. N.; Waszczak, J. V. Topochemical Reactions of Rutile Related Structures with Lithium. *Mater. Res. Bull.* **1978**, *13*, 1395−1402.

(16) Kuhn, A.; Baehtz, C.; García-Alvarado, F. Structural Evolution of Ramsdellite-Type $Li_xTi_2O_4$ upon Electrochemical Lithium Insertion−deinsertion ($0 \le x \le 2$). *J. Power Sources* **2007**, *174*, 421−427.

(17) Wiedemann, D.; Nakhal, S.; Franz, A.; Lerch, M. Lithium Diffusion Pathways in Metastable Ramsdellite-like $Li_2Ti_3O_7$ from High-Temperature Neutron Diffraction. *Solid State Ionics* **2016**, *293*, 37−43.

(18) Koudriachova, M. V. Ramsdellite-Structured $LiTiO_2$: A New Phase Predicted from Ab Initio Calculations. *Chem. Phys. Lett.* **2008**, *458*, 108−112.

(19) Abrahams, I.; Bruce, P. G.; David, W. I. F.; West, A. R. Refinement of the Lithium Distribution in $Li_2Ti_3O_7$ Using High-Resolution Powder Neutron Diffraction. *J. Solid State Chem.* **1989**, *78*, 170−177.

(20) Tarte, P.; Gabelica-Robert, M. New Complex Antimonate and Tellurates Structurally Related to Lithium Antimonate $LiSbO_3$. *C. R. Seances Acad. Sci., Vie Acad.* **1983**, *296*, 261.

(21) Pospelov, A. A.; Nalbandyan, V. B.; Serikova, E. I.; Medvedev, B. S.; Evstigneeva, M. A.; Ni, E. V.; Lukov, V. V. Crystal Structure and Properties of a New Mixed-valence Compound $LiMn_2TeO_6$ and the Survey of the $LiMM'XO_6$ Family (X = Sb or Te). *Solid State Sci.* **2011**, *13*, 1931−1937.

(22) Yuhasz, W. M. U.S. Patent 10,202,510 B2, 2019.

(23) Bergerhoff, G.; Hundt, R.; Sievers, R.; Brown, I. D. The Inorganic Crystal Structure Data Base. *J. Chem. Inf. Comput. Sci.* **1983**, *23*, 66−69.

https://dx.doi.org/10.1021/acs.chemmater.0c01491
Chem. Mater. 2020, 32, 4785−4794

(24) Belsky, A.; Hellenbrandt, M.; Karen, V. L.; Luksch, P. New Developments in the Inorganic Crystal Structure Database (ICSD): Accessibility in Support of Materials Research and Design. *Acta Crystallogr., Sect. B: Struct. Sci.* **2002**, *58*, 364−369.
(25) Kim, J.-W.; Lee, H.-G. Thermal and Carbothermic Decomposition of Na_2CO_3 and Li_2CO_3. *Metall. Mater. Trans. B* **2001**, *32*, 17−24.
(26) *SAINT V8.38A*; Bruker Analytical X-ray Instruments: Madison, WI, USA, 2016.
(27) Sheldrick, G. *SADABS*; University of Göttingen: Göttingen, Germany, 2002.
(28) Sheldrick, G. M. Crystal Structure Refinement with SHELXL. *Acta Crystallogr., Sect. C: Struct. Chem.* **2015**, *71*, 3−8.
(29) Dolomanov, O. V.; Bourhis, L. J.; Gildea, R. J.; Howard, J. a. K.; Puschmann, H. OLEX2: A Complete Structure Solution, Refinement and Analysis Program. *J. Appl. Crystallogr.* **2009**, *42*, 339−341.
(30) Spek, A. L. Single-Crystal Structure Validation with the Program PLATON. *J. Appl. Crystallogr.* **2003**, *36*, 7−13.
(31) Toby, B. H.; Von Dreele, R. B. GSAS-II: The Genesis of a Modern Open-Source All Purpose Crystallography Software Package. *J. Appl. Crystallogr.* **2013**, *46*, 544−549.
(32) Clark, S. J.; Segall, M. D.; Pickard, C. J.; Hasnip, P. J.; Probert, M. I. J.; Refson, K.; Payne, M. C. First Principles Methods Using CASTEP. *Z. Kristallogr. - Cryst. Mater.* **2005**, *220*, 567−570.
(33) Vanderbilt, D. Soft Self-Consistent Pseudopotentials in a Generalized Eigenvalue Formalism. *Phys. Rev. B: Condens. Matter Mater. Phys.* **1990**, *41*, 7892−7895.
(34) Perdew, J. P.; Burke, K.; Ernzerhof, M. Generalized Gradient Approximation Made Simple. *Phys. Rev. Lett.* **1996**, *77*, 3865−3868.
(35) Monkhorst, H. J.; Pack, J. D. Special Points for Brillouin-Zone Integrations. *Phys. Rev. B: Solid State* **1976**, *13*, 5188−5192.
(36) Pickard, C. J.; Mauri, F. All-electron Magnetic Response with Pseudopotentials: NMR Chemical Shifts Extended Systems. *Phys. Rev. B: Condens. Matter Mater. Phys.* **2001**, *63*, 245101.
(37) Yates, J. R.; Pickard, C. J.; Mauri, F. Calculation of NMR Chemical Shifts for extended systems using Ultrasoft Pseudopotentials. *Phys. Rev. B: Condens. Matter Mater. Phys.* **2007**, *76*, 024401.
(38) Profeta, M.; Mauri, F.; Pickard, C. J. Accurate First Principles Prediction of ^{17}O NMR Parameters in SiO_2: Assignment of the Zeolite Ferrierite Spectrum. *J. Am. Chem. Soc.* **2003**, *125*, 541.
(39) Sturniolo, S.; Green, T. F. G.; Hanson, R. M.; Zilka, M.; Refson, K.; Hodgkinson, P.; Brown, S. P.; Yates, J. R. Visualization and Processing of Computed Solid-State NMR Parameters: MagresView and MagresPython. *Solid State Nucl. Magn. Reson.* **2016**, *78*, 64−70.
(40) Pankove, J. I. *Optical Processes in Semiconductors*; Dover Publications: New York, 1975.
(41) Xu, X. Charge Transport across Single Grain Boundaries in Oxide Electrolytes, ProQuest Dissertations Publishing, Northwestern University, 2019, p 22618334.
(42) Fujihala, M.; Koorikawa, H.; Mitsuda, S.; Hagihala, M.; Morodomi, H.; Kawae, T.; Matsuo, A.; Kindo, K. Spin-Liquid Ground State in the Spin 1/2 Distorted Diamond Chain Compound $K_3Cu_3AlO_2(SO_4)_4$. *J. Phys. Soc. Jpn.* **2015**, *84*, 073702.
(43) Sorolla, M.; Wang, X.; Kubíčková, L.; Ksenofontov, V.; Möller, A.; Jacobson, A. J. A Mixed-Valent Iron (II/III) Diamond Chain with Single-Ion Anisotropy. *Inorg. Chem.* **2020**, *59*, 1068−1074.
(44) Hiroi, Z. Structural Instability of the Rutile Compounds and Its Relevance to the Metal−Insulator Transition of VO_2. *Prog. Solid State Chem.* **2015**, *43*, 47−69.
(45) Schmidt, W.; Wilkening, M. Discriminating the Mobile Ions from the Immobile Ones in $Li_{4+x}Ti_5O_{12}$: ^6Li NMR Reveals the Main Li^+ Diffusion Pathway and Proposes a Refined Lithiation Mechanism. *J. Phys. Chem. C* **2016**, *120*, 11372−11381.
(46) Zhang, Z.-G.; Abe, T.; Moriyoshi, C.; Tanaka, H.; Kuroiwa, Y. Study of Materials Structure Physics of Isomorphic $LiNbO_3$ and $LiTaO_3$ Ferroelectrics by Synchrotron Radiation X-Ray Diffraction. *Jpn. J. Appl. Phys.* **2018**, *57*, 11UB04.
(47) Zhang, Z.-G.; Abe, T.; Moriyoshi, C.; Tanaka, H.; Kuroiwa, Y. Synchrotron-Radiation X-Ray Diffraction Evidence of the Emergence of Ferroelectricity in $LiTaO_3$ by Ordering of a Disordered Li Ion in the Polar Direction. *Appl. Phys. Express* **2018**, *11*, 071501.
(48) Genkina, E. A. Accurate Definition of $LiSbO_3$ Crystal Structure. *Kristallografiya* **1992**, *37*, 356−358.
(49) de Wolff, P. M. Interpretation of Some Gamma-MnO_2 Diffraction Patterns. *Acta Crystallogr.* **1959**, *12*, 341.
(50) Bayer, G. $InSbO_4$ and $ScSbO_4$, New Compounds with the Rutile Structure. *Z. Kristallogr. - New Cryst. Struct.* **1963**, *118*, 158−160.
(51) Choisnet, J.; Bizo, L.; Retoux, R.; Hébert, S.; Raveau, B. New Transparent Conductors with the M_7O_{12} Ordered Oxygen-Deficient Fluorite Structure: From $In_4Sn_3O_{12}$ to $In_{5.5}Sb_{1.5}O_{12}$. *J. Solid State Chem.* **2004**, *177*, 3748−3751.
(52) Xu, K.; Xu, D.; Zhang, X.; Luo, Z.; Wang, Y.; Zhang, S. Visible-Light Activity of N-$LiInO_2$: Band Structure Modifications through Interstitial Nitrogen Doping. *Appl. Surf. Sci.* **2017**, *391*, 645−653.
(53) Goodenough, J. B. Ceramic Solid Electrolytes. *Solid State Ionics* **1997**, *94*, 17−25.
(54) *Ceramic Materials for Electronics: Processing, Properties, and Applications*; Buchanan, R. C., Ed.; Marcel Dekker Inc.: New York City; 1986; p 50.

https://dx.doi.org/10.1021/acs.chemmater.0c01491
Chem. Mater. 2020, 32, 4785−4794